JℲM RAPIDS

Shape effect on solid melting in flowing liquid

Rui Yang[1],†, Christopher J. Howland[1], Hao-Ran Liu[2], Roberto Verzicco[1,3,4] and Detlef Lohse[1,5]

[1]Physics of Fluids Group, Max Planck Center for Complex Fluid Dynamics, and J. M. Burgers Centre for Fluid Dynamics, University of Twente, P.O. Box 217, 7500AE Enschede, The Netherlands

[2]Department of Modern Mechanics, University of Science and Technology of China, Hefei 230027, PR China

[3]Dipartimento di Ingegneria Industriale, University of Rome 'Tor Vergata', Roma 00133, Italy

[4]Gran Sasso Science Institute - Viale F. Crispi, 7 67100 L'Aquila, Italy

[5]Max Planck Institute for Dynamics and Self-Organization, 37077 Göttingen, Germany

Iceberg melting is a critical factor for climate change. However, the shape of an iceberg is an often neglected aspect of its melting process. Our study investigates the influence of different ice shapes and ambient flow velocities on melt rates by conducting direct numerical simulations of a simplified system of bluff body flow. Our study focuses on the ellipsoidal shape, with the aspect ratio as the control parameter. We found the shape plays a crucial role in the melting process, resulting in significant variations in the melt rate between different shapes. Without flow, the optimal shape for a minimal melt rate is the disk (two-dimensional) or sphere (three-dimensional), due to the minimal surface area. However, as the ambient flow velocity increases, the optimal shape changes with the aspect ratio. We find that ice with an elliptical shape (when the long axis is aligned with the flow direction) can melt up to 10 % slower than a circular shape when exposed to flowing water. Following the approach considered by Huang *et al.* (*J. Fluid Mech.*, vol. 765, 2015, R3) for dissolving bodies, we provide a quantitative theoretical explanation for this optimal shape, based on the combined contributions from both surface-area effects and convective-heat-transfer effects. Our findings provide insight into the interplay between phase transitions and ambient flows, contributing to our understanding of the iceberg melting process and highlighting the need to consider the aspect-ratio effect in estimates of iceberg melt rates.

Key words: sea ice, solidification/melting

† Email address for correspondence: r.yang-1@utwente.nl

1. Introduction

With global warming, more icebergs are breaking off from Antarctica, accelerating sea level rise (Scambos *et al.* 2017). Additionally, melting icebergs and sea ice floes also contribute significantly to climate and environment change, including freshwater supply (Huppert & Turner 1978), biological productivity (Wadham *et al.* 2019) and carbon sequestration (Duprat, Bigg & Wilton 2016), making the understanding of iceberg melting rates crucial for comprehending the interplay between icebergs and the climate (Cenedese & Straneo 2023). To describe the melt rate of icebergs, different parametrization models are proposed, such as employing empirical relations for turbulent heat transfer over a flat plate to predict iceberg melt rates (Weeks & Campbell 1973), considering meltwater-plume effect on the melt rate with ambient flows (FitzMaurice, Cenedese & Straneo 2017), and coupling effects of turbulence, buoyant convection and waves (Martin & Adcroft 2010).

Various lab experiments and direct numerical simulations have been conducted to investigate the interaction between ice melting and ambient flow in the laboratory scale, including ice melting in still and flowing water (Dumore, Merk & Prins 1953; Vanier & Tien 1970; Hao & Tao 2002; Hester *et al.* 2021; Weady *et al.* 2022), in Rayleigh–Bénard convection (Davis, Müller & Dietsche 1984; Dietsche & Müller 1985; Esfahani *et al.* 2018; Favier, Purseed & Duchemin 2019; Yang *et al.* 2023*b*), which involves a plate being heated from below and a plate being cooled from above (Lohse & Xia 2010; Ecke & Shishkina 2023), and in vertical convection (Wang *et al.* 2021*c*; Yang *et al.* 2022). The density anomaly effect in freshwater, combined with inclination, causes distinct flow regimes and ice melting morphology under different temperatures, which has been comprehensively investigated by Wang, Calzavarini & Sun (2021*a*), Wang *et al.* (2021*b*,*c*). Salinity results in even more complex mushy layer structures (Worster 1997), where convection also occurs (Du *et al.* 2023). These studies highlight the complex interplay between ice melting and ambient flow, leading to distinct ice morphologies and melt rates.

Icebergs and ice floes exhibit considerable variations in shape and size (Gherardi & Lagomarsino 2015), with horizontal extents ranging from a few metres to several hundred kilometres. Despite extensive research on iceberg melt rates using models, experiments and simulations, the potential effects of the aspect ratio on the melt rate have not received much attention. One of the experimental results is that the overall melt rate strongly depends on the aspect ratio (Hester *et al.* 2021; Cenedese & Straneo 2023), which is also the motivation for our study on the aspect ratio effect on the melt rate.

Further theoretical understanding on the melting of solid objects in fluid flow can be gained from the analogy with dissolution or erosion processes. Whereas the ablation rate of a melting object is determined by the temperature gradient at the liquid–solid boundary, for dissolution this is instead the gradient of solute concentration, and for erosion it is the shear stress at the boundary. From this perspective, the underlying physics of melting and dissolution are identical, and the Reynolds analogy for passive scalar transport can be used to also draw comparisons with erosion. Ristroph *et al.* (2012) performed experiments of an erodible sphere in a uniform flow and use a simple boundary-layer model to describe the resulting self-similar shape. Moore *et al.* (2013) extended this work with further experiments and quasistatic simulations to describe how other initial shapes, including ellipses, evolve towards a self-similar shape. For dissolving objects, Huang, Moore & Ristroph (2015) use a similar boundary layer approach to describe the dissolution rate and resulting dynamical shapes. Although this series of work has made great progress in understanding the ablation rate scalings and shape evolution, the effect of the initial aspect ratio on the time taken for the object to vanish has not yet been considered. We note that a difference between melting and dissolution is the very different Prandtl respective

Schmidt number, with the latter one for dissolution typically being more than two orders of magnitude larger.

In this study, we investigate the influence of the ice shape (ellipse aspect ratio) on melt rates through numerical simulations and theoretical analysis in an idealized setting. We focus on the scenario of ice melting in a uniform flow, as detailed in §2, and neglect buoyancy effects and basal melting due to our focus on the top view of the melting process, distinguishing our work from previous studies (Couston *et al.* 2021; Hester *et al.* 2021). Our aim is to understand how the aspect ratio affects ice melt rates by conducting a series of numerical simulations in a simplified system as a fundamental problem. Our findings reveal that the aspect ratio plays a crucial role in the melting process, leading to substantial variations in melt rates. We further propose a theoretical model for the dependence of melt rates on the control parameters that agrees well with the simulation results. In this model, two contributions to the total melt rate are distinguished – surface contact-induced melt and advective flow-induced melt. The observed strong aspect ratio dependence can be quantitatively understood.

2. Numerical method and set-up

We numerically integrate the velocity field $\boldsymbol{u}$ and the temperature field θ according to the Navier–Stokes equations, neglecting the effect of buoyancy induced by temperature differences. The melting process is modelled by the phase-field method, which has been widely used in previous studies (Favier *et al.* 2019; Couston *et al.* 2021; Hester *et al.* 2021; Yang *et al.* 2022, 2023*b*). In this technique, the phase-field variable ϕ is integrated in time and space and smoothly transitions from a value of 1 in the solid to a value of 0 in the liquid. The equations are non-dimensionalized by inflow speed U_0 as the velocity scale, ice effective diameter D as the length scale, and the temperature difference between the ambient flow and the ice T_0 as the temperature scale. The non-dimensionalized quantities include three velocity components u_i with $i = 1, 2, 3$, the pressure p, the temperature θ and the phase-field scalar ϕ. The dimensionless governing equations read

$$\nabla \cdot \boldsymbol{u} = 0, \tag{2.1}$$

$$\partial_t \boldsymbol{u} + \nabla \cdot (\boldsymbol{uu}) = -\nabla p + \frac{1}{Re}\nabla^2 \boldsymbol{u}, \tag{2.2}$$

$$\partial_t \theta + \nabla \cdot (\boldsymbol{u}\theta) = \frac{1}{RePr}\nabla^2 \theta + St\partial_t\phi, \tag{2.3}$$

$$\frac{\partial \phi}{\partial t} = \frac{6}{5StCRePr}\left[\nabla^2\phi - \frac{1}{\beta^2}\phi(1-\phi)(1-2\phi+C\theta)\right], \tag{2.4}$$

where β is the diffusive interface thickness, which is typically set to be the mean grid spacing. The control parameters of the system are the Reynolds number Re, which is the dimensionless flow strength, the Prandtl number Pr, which is the ratio between kinematic viscosity ν and thermal diffusivity κ, and the Stefan number St, which is the ratio between latent heat and sensible heat, and the aspect ratio of the initial ice shape γ, which is defined as the ratio of its width and length and will be the focus of this paper:

$$Re = \frac{U_0 D}{\nu}, \quad Pr = \frac{\nu}{\kappa}, \quad St = \frac{\mathcal{L}}{c_p \Delta T}, \quad \gamma = \frac{l_w}{l_l}. \tag{2.5a–d}$$

Here, U_0 is the inflow velocity, l_w and l_l are the initial width and length of the ice shape (shown in figure 1*b*), $\mathcal{L}$ is the latent heat, c_p is the specific heat capacity, $\Delta T = T_0 - T_i$ is
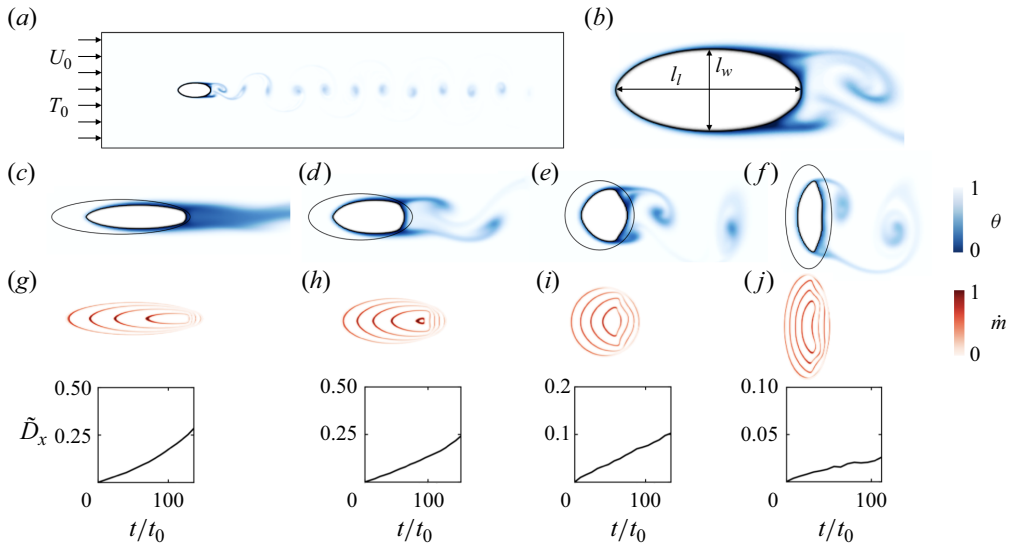
Figure 1. (*a*) An illustration of the set-up for ice melting in flowing water. The inflow is set at the left boundary with unidirectional velocity U_0 and uniform temperature T_0. (*b*) Zoomed-in view of the ice object. Here l_w and l_l represent the width and the length of the object, respectively. Panels (*c*–*f*) represent the snapshots of the temperature field of ice melting in flowing water with different aspect ratios γ, namely (*c*) $\gamma = 0.25$, (*d*) 0.44, (*e*) 1 and (*f*) 2.25. The corresponding movies are shown as supplementary movies and are available at https://doi.org/10.1017/jfm.2023.1080. Panels (*g*–*j*) show the snapshots of $\partial\phi/\partial t$ (see text for more details), corresponding to the cases in (*c*–*f*). The colour represents the local melt rate over the surface at different times. Also, the corresponding plot of the shift distance $\tilde{D}_x$ (normalized by corresponding l_l) of the centroids as a function of the dimensionless time is given. The mass loss rate $\dot{m}$, normalized $\partial\phi/\partial t$, is colour-coded.

the temperature difference between inflow temperature T_0 and the initial ice temperature T_i. Due to the large parameter space, some of the control parameters have to be fixed in order to make the study feasible. For the time being, we fix $Pr = 7$ and $St = 4$ as the values for water at 20 °C, unless specified otherwise, and $T_i = 0$ °C, the same as the melting temperature. Varying T_i presumably also affects the melting process as the temperature conduction inside the solid also plays a role, which is worth further exploration. Later we also investigate the effect of Pr and St independently. Our simulations cover a parameter range of $0 \leq Re \leq 10^3$ ($Re = 10^3$ corresponds to flow speed $U = 5$ cm s^{-1} and ice diameter $D = 2$ cm) and $0.1 \leq \gamma \leq 2.25$. Here C is the phase mobility parameters related to the Gibbs–Thompson relation. We choose $C = 1$, which may overestimate the Gibbs-Thomson effect for high curvature. Therefore we avoid too extreme values of γ, where the high curvature regions might be inaccurate. We further impose a direct forcing of the velocity to zero for $\phi > 0.9$, preventing spurious motions inside the solid phase (Howland 2022). More details can be found in previous studies (Hester *et al.* 2020; Yang *et al.* 2023*b*). Simulations are performed using the second-order staggered finite difference code AFiD, which has been extensively validated and used to study a wide range of turbulent flow problems (Ostilla-Mónico *et al.* 2015; Yang, Verzicco & Lohse 2016; Liu *et al.* 2022), including phase-change problems (Yang *et al.* 2022, 2023*b*). The phase-field method is applied to model the phase-change process, which has been widely used in previous studies (Favier *et al.* 2019; Couston *et al.* 2021; Hester *et al.* 2021; Ravichandran & Wettlaufer 2021; Yang *et al.* 2023*b*).

980 R1-4

The flow is confined vertically by two parallel boundaries with free-slip boundary conditions for the velocity and adiabatic for the temperature (see figure 1*a*). In the simulations, we prescribe an ice object with area A_0 and effective diameter $D = 2\sqrt{A_0/\pi}$ in a domain of length $L = 20D$ and width $W_z = 5D$. Both two-dimensional (2-D) ($L/W_z = 4$) and three-dimensional (3-D) simulations ($L/W_z = L/W_x = 4$) are conducted. The long and short axis lengths of the ellipse are $l_l = D/\sqrt{\gamma}$ and $l_w = D\sqrt{\gamma}$, respectively. Note that the finite cross-stream dimension of the computation domain could in principle lead to blockage effects. To ensure that this does not affect our results, we performed a test for circle shapes at $Re = 400$ with different W_z, which produced a convergent melt rate at $W_z = 5D$. Initially, the simulations are run with the ice object fixed at zero velocity and $\theta_i = 0$, and the melting process is turned off until the flow reaches the fully developed stage, then we turn on the melting process. The velocity and temperature at the left and right boundary are set as uniform U_0 and T_0 by a penalty force. The initial temperature of the ice is set as the melting temperature $\theta_i = 0$, and the ambient fluid is set as the inflow temperature $\theta = 1$. The position of the ice front is described as isocontour $\phi = 1/2$ as time evolves. Grid convergence tests are shown in figure 2.

3. Shape evolution and melt-rate dependence on parameters

We first investigate the evolution of ice shapes, which depends on the initial shape and the flow rate. Temperature fields under different initial shapes for a fixed area are shown in figure 1(*c*–*f*) (γ increases from (*c*) to (*f*)). From the temperature field, one can see the complex interaction between melting and detaching wake vortices. The ice has distinct front and back shapes – ice at the back is more deformed than at the front, due to the detaching vortices in the wake flow, which induce reduced and non-uniform heat flux.

To study the local melt rate at the ice front, we further plot $\partial\phi/\partial t$ in figure 1(*g*–*j*), whose value is zero in the solid and liquid phases. At the solid–liquid interface, its value provides insight into the local melt rate. It reveals that two parts of the ice melt faster (in reddish colour): the front due to inflow, and the back due to wake flow. This melting characteristic is similar to that of dissolution (Ristroph *et al.* 2012; Huang *et al.* 2015) and to what was formed in previous experiments on melting spheres (Hao & Tao 2002), where the front tends to melt faster than the back. This occurs because the liquid at the back of the solid is cooler than at the front due to mixing induced by the wake. We investigate the front-to-back asymmetry in the melting by plotting the distance of the ice centroid from its initial position over time in figure 1(*g*–*j*). For small γ, we observe a significant shift of the centroid to the back, while for large γ, the larger cross-section results in stronger detaching flow, which enhances melting at the back and thus prevents a significant movement of the centroid (see figure 1*f*). As melting progresses, the front of the shape remains rounded, and different back shapes are obtained for different γ. These shapes can be attributed to the presence of the detaching vortices, whose shedding occurs in an oscillating manner at the top and bottom of the body. As a result, melting is favoured at the top and bottom, creating a wedge-like shape. It is also interesting to note that earlier works emphasized that the front shape of eroding/dissolving bodies converges to a terminal form (Ristroph *et al.* 2012; Huang *et al.* 2015). Here we observed that slender bodies are blunted and blunt bodies are made slender. The front shapes of different bodies become similar as they melt, but they completely melt before the stage where they may converge to a terminal form.

The complicated ice–water interaction affects not only the melting shape but also the melt rate. Figure 3(*a*) shows the normalized total area change over time for different aspect ratio γ. For increasing γ, the melt curves exhibit a non-monotonic trend, with the melt rate first decreasing and then increasing. We measure the time taken for the ice to completely
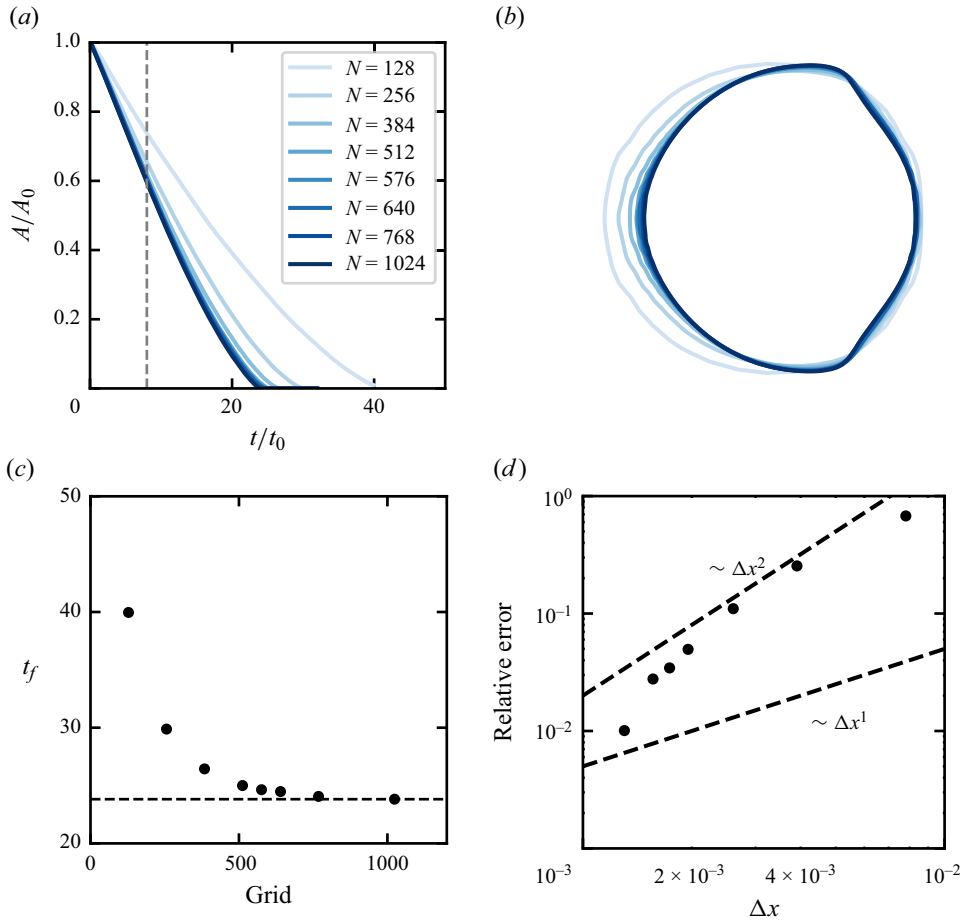
Figure 2. Resolution convergence test. (*a*) The normalized area as a function of dimensionless time for different resolutions at $Re = 400$. (*b*) The contour plots of the ice surface at $t = 8t_0$ (grey dashed line in (*a*)). (*c*) Calculated t_f as a function of the grid resolution. The dashed line shows the value of t_f for the highest resolution we run. Based on this, our final choice of the resolution N of the cross-section length for $Re = 400$ is $N = 576$. (*d*) The relative convergence test. The y-axis is the relative error $|t_f - t_{f_0}|/t_{f_0}$ where t_{f_0} is the t_f for the highest resolution. The dashed lines represent the linear and quadratic relations.

melt as t_f, and take $\bar{f} = 1/t_f$ to be the mean melt rate. Figure 3(*b*) shows the normalized melt rate $\bar{f}/f_0$ as a function of γ for different Re, where $f_0(Re)$ is the mean melt rate for the circles ($\gamma = 1$). Here, the same trend is observed, and $\bar{f}$ depends not only on γ but also on Re. In the absence of flow ($Re = 0$), the minimum melt rate occurs at the optimal aspect ratio $\gamma_{min} = 1$ for a circle shape. As Re increases, γ_{min} decreases until it converges to approximately $\gamma_{min} \approx 0.5$. The same trend is also observed for 3-D simulations of a cylinder with the cross-section of different aspect ratios.

Our findings demonstrate that ice with an elliptical shape (when the long axis is aligned with the flow direction) can melt up to 10 % slower than a circle shape when exposed to flowing water. This previously neglected shape factor may have implications for accurately estimating the melt rate of icebergs in previous models that neglected it (Weeks & Campbell 1973; Martin & Adcroft 2010; FitzMaurice *et al.* 2017). The non-intuitive nature of this phenomenon raises a further question about its physical mechanism.
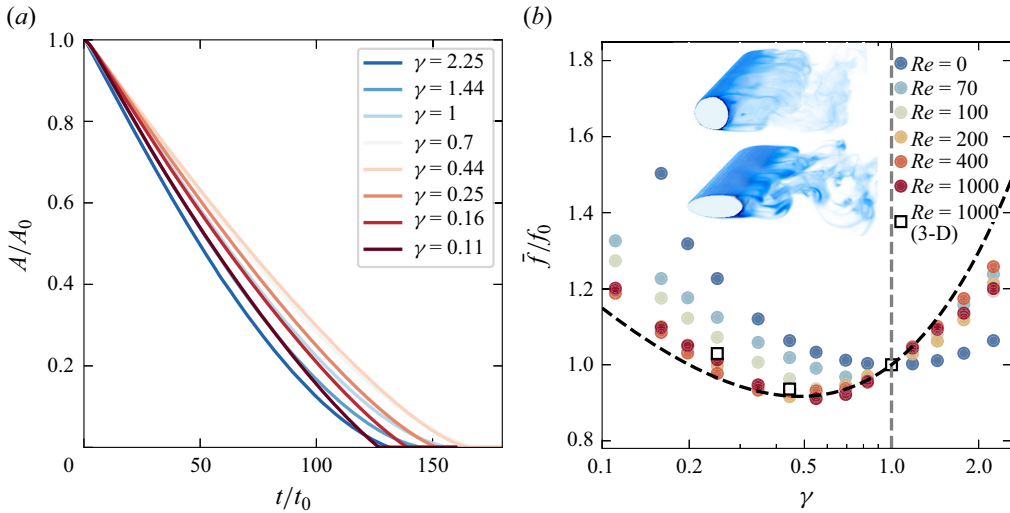
980 R1-6

Figure 3. (*a*) The area A normalized A_0 as function of time normalized by $t_0 = D/U_0$ for different γ and fixed $Re = 10^3$, $Pr = 7$ and $St = 4$. (*b*) Overall melt rate $\bar{f}/f_0$ (from initial to complete melt), normalized by the overall melt rate f_0 at $\gamma = 1$, as a function of γ for different Re. The inset image shows the snapshots of temperature fields for 3-D simulation results ($Re = 10^3$). The dashed line is the theoretical curve from (4.6), which is expected to hold for larger Re.

4. Theoretical model for the melt rate

To quantitatively explain the result, we follow the same approach as used by Ristroph *et al.* (2012) and Huang *et al.* (2015) for eroding or dissolving bodies and consider the total ice mass budget for the melting process:

$$\frac{dA(t)}{dt} = P(\gamma, t) v_n, \tag{4.1}$$

where $P(\gamma, t)$ is the perimeter of the ice (for 2-D), and $v_n(t)$ is the surface-averaged melt speed. Assuming the elliptical shape is not significantly changing with time (i.e. $\gamma(t) \approx \gamma(t = 0) = \gamma$), we have the expression for the ellipse perimeter from the elliptic integral:

$$P(\gamma, t) = 2\sqrt{\frac{A(t)}{\pi\gamma}} \int_0^{2\pi} \sqrt{1 - (1 - \gamma^2)\sin^2\alpha}\, d\alpha, \tag{4.2}$$

where α is the angle. Here $v_n(t)$ would be uniform everywhere in the absence of flow. The presence of a flow around the body increases the temperature gradient at the ice front which enhances the heat transfer and also makes $v_n(t)$ non-uniform as $v_n(\alpha, t)$. The flow creates a viscous boundary layer and a thermal boundary layer, respectively of thicknesses δ_v and δ_θ. The width ratio of the boundary layers is given by the Prandtl number; $Pr = \nu/\kappa = 7$ in our case implies $\delta_v > \delta_\theta$, as illustrated in figure 4(*a,b*). In order to understand the coupling between the shape of the object and the flow around it, we consider the Stefan boundary condition, i.e. the (dimensionless) surface-averaged melt speed $\tilde{v}_n$ is related to the surface-averaged heat flux $\overline{Nu}$:

$$\tilde{v}_n = \frac{v_n}{U_0} = -\frac{1}{U_0}\frac{\kappa c_p}{\mathcal{L}}\frac{\partial T}{\partial n} = \frac{\overline{Nu}}{StPrReA^{1/2}}, \tag{4.3}$$

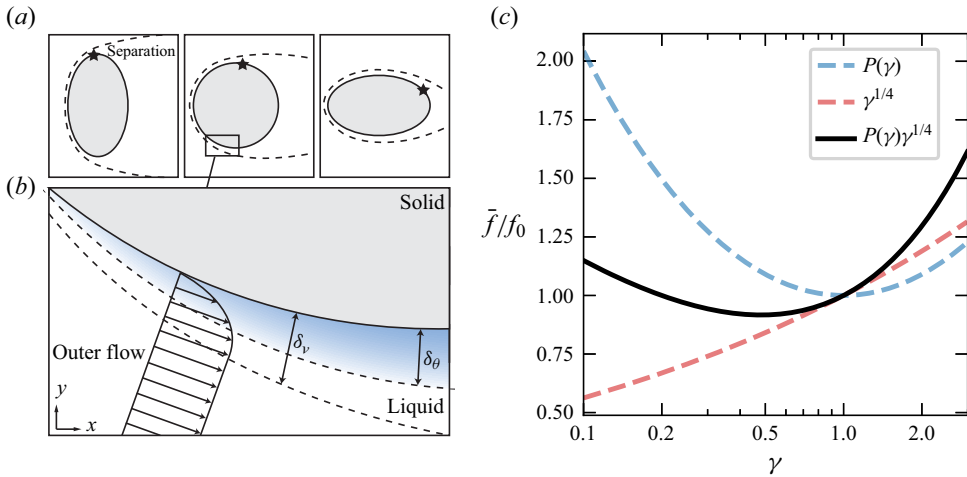**980** R1-7

Figure 4. (*a*). A schematic of the flow and temperature fields for different γ. The steady outer flow consists of warm water, while the attached flow near the body forms a boundary layer (dashed line) containing the melted fluid. It also shows that the separation point of flow moves downstream as γ decreases. (*b*) Zoomed-in view of the velocity and temperature boundary layers, the former defined by the velocity and the latter by the temperature gradient. (*c*) The theoretical curve from (4.6), including $P(\gamma)$, $\epsilon^{1/4}$ and $P(\gamma)\gamma^{1/4}$ as a function of γ. Here, $Pr = 7$, $St = 4$.

where we can use the relation from the well-known scaling of thermal boundary-layer thickness (Meksyn 1961; Grossmann & Lohse 2004) for the laminar boundary layer:

$$\overline{Nu} \sim \delta_\theta^{-1} \sim Re_{l_w}^{1/2} Pr^{1/3}/C(Pr), \tag{4.4}$$

with $Re_{l_w} = l_w U/\nu$ the Reynolds number defined by the cross-section length $l_w = 2\sqrt{\gamma A/\pi}$, $C(Pr)$ is an infinite alternating series given in Meksyn (1961). In the limit of large Pr, the series for $C(Pr)$ will converge to $C(Pr) = 1$. By substituting equations (4.2) and (4.3) into (4.1), we obtain an ordinary differential equation which is easily solved, with the result

$$A(t) = A_0 \left(1 - \frac{t}{t_f}\right)^{4/3}, \tag{4.5}$$

$$t_f^{-1} \sim P(\gamma)\gamma^{1/4} \frac{Pr^{-2/3}}{C(Pr)} St^{-1}. \tag{4.6}$$

The 4/3 scaling of (4.5) is identical to that derived by Ristroph *et al.* (2012) and Moore *et al.* (2013) for eroding bodies, and the time to fully melt (4.6) is similar to the expression obtained by Huang *et al.* (2015) in the case of dissolution, though there Prandtl/Schmidt number is more than two orders of magnitude larger. The additional novelty of (4.6) is in the dependence on the aspect ratio γ, which arises from including such dependence in the Reynolds number used in (4.4). This dependence is the focus of this work.

From (4.6) the overall melt rate $\bar{f}$ depends on γ as $\bar{f} = t_f^{-1} \sim P(\gamma)\gamma^{1/4}$, where $\gamma^{1/4}$ originates from the scaling of $\overline{Nu}$, representing the advective flow-induced melt, and $P(\gamma)$ represents the surface contact-induced melt. The contributions of $P(\gamma)$ and $\gamma^{1/4}$ are both presented in figure 4(*b*), with $P(\gamma)$ exhibiting a symmetric curve as a function of γ with a minimum at $\gamma = 1$, which represents melting without flow. In contrast, $\gamma^{1/4}$ displays a monotonic increase in melt rate, indicating that ambient flow enhances melt rate.
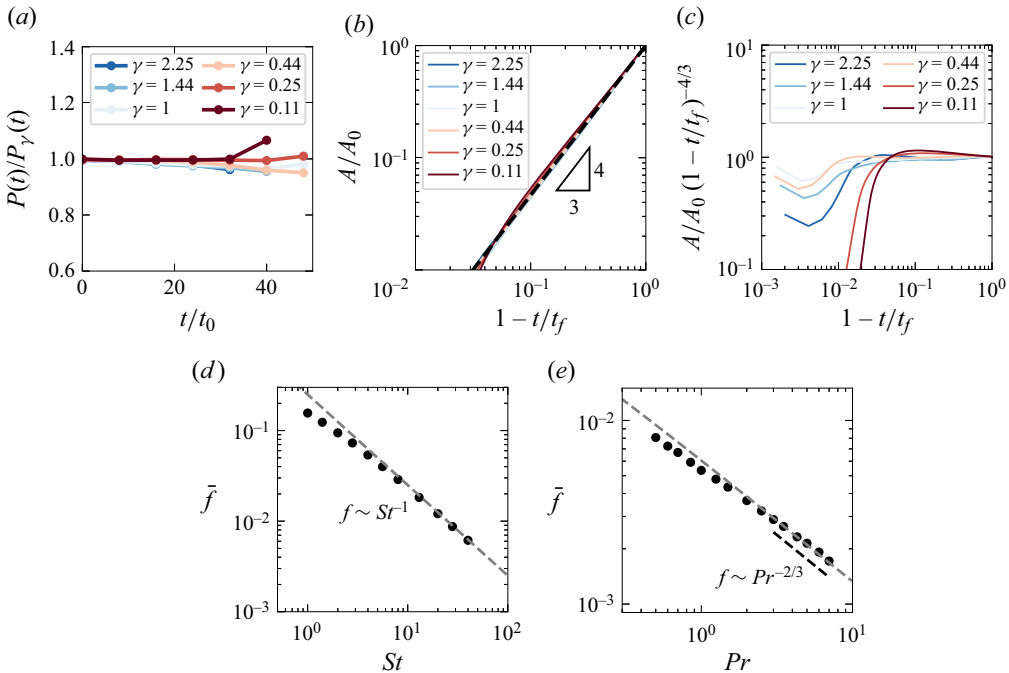
Figure 5. (*a*) The ratio between the measured perimeter from simulations and the ideal elliptical perimeter from (4.2) for varying γ at $Re = 400$. The ratio close to 1 means that our assumption is valid. (*b*) The normalized area A/A_0 as a function $1 - t/t_f$ for varying γ at $Re = 400$. All curves follow the 4/3 scaling as theoretically derived in (4.5). (*c*) The compensated plot of the normalized area $A/A_0(1 - t/t_f)^{-4/3}$ as a function $1 - t/t_f$ for varying γ at $Re = 400$. (*d*) The melt rate as a function of St for fixed $\gamma = 1$. The dashed grey line represents $\bar{f} \sim St^{-1}$. (*e*) The melt rate as a function of Pr for fixed $\gamma = 1$. The dashed grey line represents $\bar{f} \sim Pr^{-2/3}/C(Pr)$.

The overall melt rate $\bar{f} \sim P(\gamma)\gamma^{1/4}$ has a non-monotonic trend with γ, with a minimum at $\gamma_{min,theory} = 0.48$ (which is essentially the same as the value $\gamma_{min,sim} \simeq 0.5$ observed by our numerical simulations). Figure 3(*b*) shows the total melt-rate curve, which agrees well with the numerical results obtained at high Re in our numerical results. For relatively low Re and even $Re = 0$, the advective flow is weak, meaning $\overline{Nu}$ is close to 1, instead of satisfying the boundary-layer relation (4.4).

In summary, the non-monotonic relation and shift of the minimum melt-rate point are physically explained by the combined contributions from the melt driven by surface contact and the melt driven by the advective flow. The former is related to the surface area, with the minimum at $\gamma = 1$, while the latter is driven by the ambient flow, leading to a monotonic increase in melt rate with increasing γ. We confirmed that the assumption of a fixed shape as the ice melts is valid by comparing the measured and calculated perimeters from (4.2) in figure 5(*a*). The ratio remains close to 1, except for large γ, which is attributed to the strong wake flow (see figure 1*f*). The deviation of the assumption at large γ also explains the deviation in figure 3(*b*) at large γ.

5. Melt rate scalings – comparison of theory and numerical result

In order to test the scaling law $A(t) \sim (1 - t/t_f)^{4/3}$ derived in the previous section, we conducted simulations with varying γ and fixed $Re = 10^3$, $Pr = 7$ and $St = 4$.

The evolution of the area of the object is depicted in figure 5(*b*), along with the scaling law given by (4.5). The trends from simulations for different γ all follow the 4/3 scaling, in agreement with the theoretical result. Our findings demonstrate that regardless of the different physical mechanisms causing the body to ablate, whether it be through erosion (Ristroph *et al.* 2012), dissolution (Huang *et al.* 2015) or melting, the scaling laws associated with the vanishing of the body are analogous.

Besides the dependence of the melt rate on γ, we can also obtain the scaling dependence of the melt rate on *Pr* and *St* from (4.6). To validate this scaling law, we performed simulations with varying *St* in figure 5(*c*) while keeping γ fixed at 1 and *Pr* fixed at 7. At large *St* (relevant for icebergs melting in cold water), the melt rate from simulation results follows $\bar{f} \sim St^{-1}$, which is consistent with the scaling law from (4.6). At small *St*, the scaling deviates from St^{-1}. It could be because ice melts so fast that the melted fluid is still surrounding the ice, regardless of the ambient flow. This trend has also been observed in the study of melting in convection (Favier *et al.* 2019). Another possible reason is that as the solid melts and the size decreases, the curvature term affects the surface melt temperature, which can cause heat diffusion inside the solid and affect the heat flux, thus the departure from the St^{-1} scaling. It has a more obvious effect for low *St* because the melt is so fast that the size of the solid quickly decreases. However, in most of our simulations and most of realistic cases, e.g. ice melting, we have $St > 1$, where St^{-1} scaling agrees well. We also conducted simulations with varying *Pr* in figure 5(*c*) while keeping γ fixed as 1 and *St* fixed as 4. The simulation results follow $\bar{f} \sim Pr^{-2/3}/C(Pr)$ from (4.6), implying a simplified scaling $\bar{f} \sim Pr^{-2/3}$ for large *Pr*, which agrees with our results. In brief, our simulation results for varying *St* and *Pr* both show good agreement with the scaling law derived in (4.6).

6. Conclusions and outlook

Through a combination of simulations and theoretical modelling, we conducted a comprehensive investigation of the melting dynamics of a disk/elliptical shape of ice immersed in a uniform flow, taking into account the coupled dynamics between flow and ice melting for various initial shapes. Our results demonstrate that in the presence of an incoming flow, the front keeps a rounded shape during the melting process, while the back of the ice exhibits different shapes depending on the initial shape. Our simulations reveal that the presence of detaching vortices behind the ice plays a crucial role in shaping the melting pattern of the object.

Furthermore, we observed that the shape of the ice also has a significant effect on the melt rate. In the absence of flow, the circular shape ($\gamma = 1$) melts more slowly than other elliptical shapes $\gamma \neq 1$. However, in the presence of an external flow, some elliptic cylindrical bodies ($\gamma < 1$) melt less rapidly than circular cylinders with the same volume. This optimal aspect ratio depends on the flow strength, represented by *Re*. Our physical understanding of this dependence of the melt rate on the initial aspect ratio comes from the combined contributions from both the surface-contact-induced melt ($\sim P(\gamma)$) and the advective-flow-induced melt ($\sim \gamma^{1/4}$). By assuming a laminar boundary layer, we obtained a model ((4.5) and (4.6)), accurately predicting the overall melt rate and its scaling as a function of γ, *Pr* and *St*. Note that the Gibbs–Thomson curvature term is constantly increasing over time as the ice melts, which may affect the estimate of t_f. But the trend of the melt rate dependence on γ should be the same, as we consider the relative melt rate for different γ compared with the disk. Our findings provide insight into the rich coupling dynamics between the ice–water interface and ambient flows and demonstrate the importance of considering ice shape in predicting melting rates,

advancing the understanding of previous studies (Hao & Tao 2002; Ristroph *et al.* 2012; Moore *et al.* 2013; Huang *et al.* 2015). Though the present setting has many idealizations, we believe there is scientific importance for our study as an interesting and non-intuitive fundamental finding that the circle does not always melt the slowest. More factors will be gradually added, such as the gravity effect, salinity effect, and their combinations, which we will investigate in the next step.

Beyond the elliptical shape we explored in this study, it would be interesting to explore a wider range of shapes to find the optimal one. The results could be sensitive to the initial shape since flow separation is an important factor. From the shape progression images of figure 1, the fastest melt rates occur in the front where the boundary-layer flow is attached to the body, while the back region in the separated wake melts more slowly. Therefore, a shape that triggers separation earlier without strongly changing the cross-section could melt more slowly. The approach employed in this study, which combines fully resolved direct numerical simulations and theoretical explanations, offers the possibility to explain other phase-change problems coupled with advective flows. We caution that our findings reveal only a subset of the numerous factors that influence the ice–water system dynamics. In future investigations, it would be worthwhile to further explore additional factors such as the buoyancy force (Favier *et al.* 2019; Couston *et al.* 2021; Wang *et al.* 2021*b*; Yang *et al.* 2023*b*), melting near sidewalls or basal walls in the presence of ambient flow, and the effect of dissolved salt (Huppert & Turner 1978; Du *et al.* 2023; Yang *et al.* 2023*a*). These topics have significant relevance to the modelling of geophysical and climatological large-scale processes. Additionally, we plan to investigate the interaction between the motion of solid objects and phase change, as this holds significant potential for further exploration since icebergs can move and rotate.

Author ORCIDs.
- Rui Yang https://orcid.org/0000-0002-9870-6743;
- Christopher J. Howland https://orcid.org/0000-0003-3686-9253;
- Hao-Ran Liu https://orcid.org/0000-0001-7754-9454;
- Roberto Verzicco https://orcid.org/0000-0002-2690-9998;
- Detlef Lohse https://orcid.org/0000-0003-4138-2255.

REFERENCES

CENEDESE, C. & STRANEO, F. 2023 Icebergs melting. *Annu. Rev. Fluid Mech.* **55**, 377–402.

COUSTON, L.-A., HESTER, E., FAVIER, B., TAYLOR, J.R., HOLLAND, P.R. & JENKINS, A. 2021 Topography generation by melting and freezing in a turbulent shear flow. *J. Fluid Mech.* **911**, A44.

DAVIS, S.H., MÜLLER, U. & DIETSCHE, C. 1984 Pattern selection in single-component systems coupling Bénard convection and solidification. *J. Fluid Mech.* **144**, 133–151.

DIETSCHE, C. & MÜLLER, U. 1985 Influence of Bénard convection on solid–liquid interfaces. *J. Fluid Mech.* **161**, 249–268.

DU, Y., WANG, Z., JIANG, L., CALZAVARINI, E. & SUN, C. 2023 Sea water freezing modes in a natural convection system. *J. Fluid Mech.* **960**, A35.

DUMORE, J., MERK, H. & PRINS, J. 1953 Heat transfer from water to ice by thermal convection. *Nature* **172** (4375), 460–461.

DUPRAT, L.P., BIGG, G.R. & WILTON, D.J. 2016 Enhanced Southern Ocean marine productivity due to fertilization by giant icebergs. *Nat. Geosci.* **9** (3), 219–221.

ECKE, R.E. & SHISHKINA, O. 2023 Turbulent rotating Rayleigh–Bénard convection. *Annu. Rev. Fluid Mech.* **55**, 603–638.

ESFAHANI, B.R., HIRATA, S.C., BERTI, S. & CALZAVARINI, E. 2018 Basal melting driven by turbulent thermal convection. *Phys. Rev. Fluids* **3** (5), 053501.

FAVIER, B., PURSEED, J. & DUCHEMIN, L. 2019 Rayleigh–Bénard convection with a melting boundary. *J. Fluid Mech.* **858**, 437–473.

FITZMAURICE, A., CENEDESE, C. & STRANEO, F. 2017 Nonlinear response of iceberg side melting to ocean currents. *Geophys. Res. Lett.* **44** (11), 5637–5644.

GHERARDI, M. & LAGOMARSINO, M.C. 2015 Characterizing the size and shape of sea ice floes. *Sci. Rep.* **5** (1), 1–11.

GROSSMANN, S. & LOHSE, D. 2004 Fluctuations in turbulent Rayleigh–Bénard convection: the role of plumes. *Phys. Fluids* **16** (12), 4462–4472.

HAO, Y.L. & TAO, Y.X. 2002 Heat transfer characteristics of melting ice spheres under forced and mixed convection. *J. Heat Transfer* **124** (5), 891–903.

HESTER, E.W., COUSTON, L.-A., FAVIER, B., BURNS, K.J. & VASIL, G.M. 2020 Improved phase-field models of melting and dissolution in multi-component flows. *Proc. R. Soc.* A **476** (2242), 20200508.

HESTER, E.W., MCCONNOCHIE, C.D., CENEDESE, C., COUSTON, L.-A. & VASIL, G. 2021 Aspect ratio affects iceberg melting. *Phys. Rev. Fluid* **6** (2), 023802.

HOWLAND, C.J. 2022 AFiD-MuRPhFi documentation. Available at: https://chowland.github.io/AFiD-MuRPhFi/.

HUANG, J.M., MOORE, M.N.J. & RISTROPH, L. 2015 Shape dynamics and scaling laws for a body dissolving in fluid flow. *J. Fluid Mech.* **765**, R3.

HUPPERT, H.E. & TURNER, J.S. 1978 On melting icebergs. *Nature* **271** (5640), 46–48.

LIU, H.-R., CHONG, K.L., YANG, R., VERZICCO, R. & LOHSE, D. 2022 Heat transfer in turbulent Rayleigh–Bénard convection through two immiscible fluid layers. *J. Fluid Mech.* **938**, A31.

LOHSE, D. & XIA, K. 2010 Small-scale properties of turbulent Rayleigh-Bénard convection. *Annu. Rev. Fluid Mech.* **42** (1), 335–364.

MARTIN, T. & ADCROFT, A. 2010 Parameterizing the fresh-water flux from land ice to ocean with interactive icebergs in a coupled climate model. *Ocean Model.* **34** (3-4), 111–124.

MEKSYN, D. 1961 *New Methods in Laminar Boundary-Layer Theory*. Pergamon.

MOORE, M.N., RISTROPH, L., CHILDRESS, S., ZHANG, J. & SHELLEY, M.J. 2013 Self-similar evolution of a body eroding in a fluid flow. *Phys. Fluids* **25** (11), 116602.

OSTILLA-MÓNICO, R., YANG, Y., VAN DER POEL, E.P., LOHSE, D. & VERZICCO, R. 2015 A multiple-resolution strategy for direct numerical simulation of scalar turbulence. *J. Comput. Phys.* **301**, 308–321.

RAVICHANDRAN, S. & WETTLAUFER, J.S. 2021 Melting driven by rotating Rayleigh–Bénard convection. *J. Fluid Mech.* **916**, A28.

RISTROPH, L., MOORE, M.N., CHILDRESS, S., SHELLEY, M.J. & ZHANG, J. 2012 Sculpting of an erodible body by flowing water. *Proc. Natl Acad. Sci.* **109** (48), 19606–19609.

SCAMBOS, T.A., *et al.* 2017 How much, how fast?: a science review and outlook for research on the instability of Antarctica's Thwaites Glacier in the 21st century. *Glob. Planet. Change* **153**, 16–34.

VANIER, C.R. & TIEN, C. 1970 Free convection melting of ice spheres. *AIChE J.* **16** (1), 76–82.

WADHAM, J.L., HAWKINGS, J., TARASOV, L., GREGOIRE, L., SPENCER, R., GUTJAHR, M., RIDGWELL, A. & KOHFELD, K. 2019 Ice sheets matter for the global carbon cycle. *Nat. Commun.* **10** (1), 3567.

WANG, Z., CALZAVARINI, E. & SUN, C. 2021*a* Equilibrium states of the ice-water front in a differentially heated rectangular cell (a). *Europhys. Lett.* **135** (5), 54001.

WANG, Z., CALZAVARINI, E., SUN, C. & TOSCHI, F. 2021*b* How the growth of ice depends on the fluid dynamics underneath. *Proc. Natl Acad. Sci.* **118**, 10.

WANG, Z., JIANG, L., DU, Y., SUN, C. & CALZAVARINI, E. 2021*c* Ice front shaping by upward convective current. *Phys. Rev. Fluid* **6** (9), L091501.

WEADY, S., TONG, J., ZIDOVSKA, A. & RISTROPH, L. 2022 Anomalous convective flows carve pinnacles and scallops in melting ice. *Phys. Rev. Lett.* **128** (4), 044502.

Weeks, W.F. & Campbell, W.J. 1973 Icebergs as a fresh-water source: an appraisal. *J. Glaciol.* **12** (65), 207–233.

Worster, M.G. 1997 Convection in mushy layers. *Annu. Rev. Fluid Mech.* **29** (1), 91–122.

Yang, R., Chong, K.L., Liu, H.-R., Verzicco, R. & Lohse, D. 2022 Abrupt transition from slow to fast melting of ice. *Phys. Rev. Fluid* **7** (8), 083503.

Yang, R., Howland, C.J., Liu, H.-R., Verzicco, R. & Lohse, D. 2023*a* Ice melting in salty water: layering and non-monotonic dependence on the mean salinity. *J. Fluid Mech.* **969**, R2.

Yang, R., Howland, C.J., Liu, H.-R., Verzicco, R. & Lohse, D. 2023*b* Morphology evolution of a melting solid layer above its melt heated from below. *J. Fluid Mech.* **956**, A23.

Yang, Y., Verzicco, R. & Lohse, D. 2016 From convection rolls to finger convection in double-diffusive turbulence. *Proc. Natl Acad. Sci.* **113**, 69–73.